Energy-Tunable Photocatalysis by Hot Carriers Generated by Surface Plasmon Polaritons

Journal:	*Journal of Materials Chemistry A*
Manuscript ID	TA-ART-12-2018-012304.R1
Article Type:	Paper
Date Submitted by the Author:	29-Jan-2019
Complete List of Authors:	Ahn, Wonmi; U.S. Naval Research Laboratory Vurgaftman, Igor ; U.S. Naval Research Laboratory Pietron, Jeremy; U.S. Naval Research Laboratory Pehrsson, Pehr ; U.S. Naval Resesarch Laboratory Simpkins, Blake; U.S. Naval Reserach Laboratory

Energy-Tunable Photocatalysis by Hot Carriers Generated by Surface Plasmon Polaritons

*Wonmi Ahn,[1] Igor Vurgaftman,[2] Jeremy J. Pietron,[3] Pehr E. Pehrsson,[3] and Blake S. Simpkins[3],**

[1]National Research Council Postdoctoral Associate, U.S. Naval Research Laboratory, Washington, DC 20375, United States, [2]Optical Sciences Division, U.S. Naval Research Laboratory, Washington, DC 20375, United States, [3]Chemistry Division, U.S. Naval Research Laboratory, Washington, DC 20375, United States

Noble metals capable of generating hot carriers by plasmon decay promote efficient charge separation with visible light, which opens a new prospect in the fields of photocatalytic energy conversion and solar fuel generation. Recent studies also indicate that by tuning system parameters such as photon energy and plasmon resonance, hot carriers may be injected into specific anti-bonding orbitals of an adsorbed molecule, making it possible for selective photocatalysis. Although numerous metal nanoparticle systems have been devised to harness plasmon-induced hot carriers, little is known for surface plasmon polariton (SPP)-induced hot carrier generation, especially for energy-tunable photocatalysis. In fact, nanoparticles' morphological variations, resonance inhomogeneity, and limited spectral tunability have challenged efficient control over energy-tunable photocatalysis. In this study, we investigated the energy-tunable photocatalysis using SPP-supporting metal film systems including a metal – semiconductor heterofilm (Ag/TiO_2) and a bare metal film (Au) by measuring electrochemical responses under a continuously-tuned illumination angle. We found that photon-to-carrier conversion efficiency measured in the heterofilm was strongly dependent on photon energy, showing a good agreement with a Schottky transport model. We also found that hot carriers generated in the bare metal film are energetically positioned near the metal's Fermi level, and therefore, chemical reactions can be controlled by tuning electrode potential or solution pH. These results demonstrate that the SPP system could provide a platform for understanding charge transport

mechanisms in plasmon-induced photocatalysis and pave a new path for energy-tunable chemical reactions.

Introduction

Gaining control over reaction rates and/or end products is a difficult, and treasured, goal in heterogeneous photocatalysis.[1,2] Conventional semiconductor photocatalysis, for example, has suffered from a considerably low product selectivity due to the high-energy photons required to create charge carriers in wide band-bap semiconductors such as TiO_2 (band-gap of ~3.2 eV), ZnO (~3.2 eV), and Bi_2O_3 (~2.8 eV).[3] In addition to the dearth of UV radiation in the solar spectrum, use of these high-energy photons could result in thermally-induced side reactions or generate free radical intermediates,[4,5] further reducing selectivity in photocatalysis. There have been efforts to increase the product selectivity in semiconductor photocatalysis by enhancing the absorption of visible-light. Examples include the doping of metal oxides with heteroatoms such as nitrogen or sulfur,[6,7] or sensitization of metal oxides with organic dyes[8] or quantum dots

(QDs).[9] The former creates a new electron donor level above the valence band of the semiconductor facilitating electron transfer to the conduction band under visible light irradiation. The latter works in a similar fashion to dye-sensitized solar cells, where excited carriers, photogenerated within the dyes or QDs, are transferred to the oxide for catalysis. However, in these examples, the energy of the reactive carrier is still fixed by the conduction band of the metal-oxide, limiting the range of carrier energies that may be attained and therefore the course of redox chemistry.

Recently, it has been demonstrated that plasmon-induced photocatalysis is capable of controlling reaction rates and/or products with hot carriers generated by visible-light.[10,11,12,13,14,15,16,17,18] Upon illumination by visible-light, noble metal nanoparticles support resonant electron oscillations on their surfaces, known as localized surface plasmons (LSPs). These excitations last only tens of femtoseconds,[19] at which time LSPs decay either radiatively, or more often, non-radiatively, through the processes such as phonon-assisted lattice scattering and Landau damping.[20] The non-radiative plasmon decay generates energetic ‘hot’ electrons and holes, which can be injected into proximal oxides or molecular systems to drive chemical reactions[21] or generate photocurrents.[22] Theoretical works have shown that the distribution of hot carriers is strongly dependent on the electronic band structure of the metal,[23,24,25] the energy of the photon,[23,24] and the shape and size of metal nanostructures.[26,27] While the band structure of the metal is a material's intrinsic property that is difficult to modify in its native form, the photon energy and LSP resonances can be conveniently tuned by the choice of excitation energy and the morphological variations of the nanoparticles.[28] Tuning the photon energy or LSP resonances also allows hot carriers to be injected into specific anti-bonding orbitals of an adsorbed molecule,[11,12,29,30,31,32] opening the possibility for selective visible-light photocatalysis by plasmon-induced hot carriers.

However, understanding the mechanisms of the plasmon-mediated photocatalysis can be challenging in the LSP-based nanoparticle systems. Most nanoparticle-based systems show large morphological variations that result in resonance inhomogeneity,[33,34] and this may obscure the relationship between the distributions of hot-carrier energies and specific reaction pathways. Reducing agents or surfactants used during synthesis of metal nanoparticles are still attached onto the metal surface[35,36] and may affect the chemical reactions under examination.

Furthermore, nanoparticle-based systems require synthesis of a wide range of nanoparticles in order to achieve LSP resonance tuning.[37] The optical resonance of plasmonic nanoparticles can be tuned by functionalizing them with polymers,[38] dopants,[39] and biomolecules,[40] but these additions would also likely alter the chemical processes under investigation. A lack of continuous resonance tunability in a given nanoparticle system limits the choice of redox chemistry, while continuous resonance tunability would provide great versatility in the hot-carrier based photocatalysis.

To address these challenges, we have recently demonstrated hot carrier-driven chemistry utilizing traveling surface plasmon polaritons (SPPs), which are homogeneous in-plane, generate uniform electric fields on a surfactant-free metal film, and provide a single sample that supports a range of plasmon energies accessible through angle-tuning.[41] Metal – semiconductor heterostructures (*i.e.*, Au/TiO_2 and Ag/TiO_2) were used in which SPP decay created hot carriers that drove solution-based oxidation of methanol and the anodic half-reaction of water-splitting. A direct correlation between photovoltage and SPP resonance confirmed that the OH^- oxidation reaction is a hot carrier-driven process rather than a plasmonic heating effect. Thus, we have verified that our SPP system with a broad and continuous spectral tunability is potentially applicable to the generation of hot carriers and plasmon-induced photocatalysis.

However, photon-to-carrier conversion efficiencies obtained with two select excitation energies at 1.6 and 2.3 eV were not enough to identify charge transfer mechanisms in the metal – semiconductor heterostructure, and the prospect of selective chemical reaction using the SPP system was largely missing.[41] In the current study, we expand our efforts for driving solution chemistry controlled through tuning the excitation energy across a wide range of wavelength, solution pH, and electrode potential. Not only did we utilize energy-tunable carrier generation and injection from the plasmonic metal into a catalytic semiconductor using a metal – semiconductor heterostructure (Ag/TiO_2), but we also studied direct charge transfer from the bare metal to a reactive species in solution using a bare plasmonic metal film (Au). In the Ag/TiO_2 heterostructure, the dependence of charge transfer efficiency on excitation energy (ranging from 1.6 to 2.4 eV) and incident angle revealed a Schottky-mediated charge transfer mechanism. In the oxide-free Au film, solution pH and electrode potentials were varied to systematically tune redox energy levels relative to the working electrode (Au film) enabling evaluation of the influence of potential alignment on hot carrier injection from the metal directly into reactive surface species. This work significantly extends our earlier proof of concept of SPP-induced photocatalysis by (i) using the SPP's inherent tunability to reveal charge transport mechanisms, (ii) comparing the differing mechanisms at work in hetero- and homostructures, and (iii) demonstrating methods for controlling transport of plasmonic hot carriers by tuning energy levels with solution pH and bias. These steps support the pursuit of selective plasmon-induced chemistry, which may find applications in important chemical reactions such as solar fuel generation, degradation of organic compounds, synthesis of new materials, and more.

Results and discussion

Surface Plasmon Polariton-Enabled Photocatalysis Systems. Figure 1a shows a schematic diagram of the SPP-supporting electrochemical cell that enables both optical and electrochemical interrogation of plasmon-mediated chemistry. The Kretschmann geometry was used to launch SPPs at the plasmonic metal film (Au or Ag; 40 nm thickness) – dielectric interface using a high-index hemispherical lens (*n* = 2.0). In order to create metal – semiconductor heterostructures, a TiO_2 film (10±3 nm thickness) was deposited *via* atomic layer deposition (ALD) on top of a Ag film. ALD is based on the sequential chemical reactions of precursors on the substrate while all the reaction byproducts are purged with inert gas such as nitrogen, enabling the deposition of pinhole-free oxide layers even on high aspect ratio nanostructures.[42] Atomic force microscope images[41] showed that the 10 nm-thick TiO_2 film is uniformly coated on the metal surface without signs of pinholes or island formation, which would cause oxidation of the metal film. We used the Ag film here because its SPP resonance spans a wider energy range in the visible than does Au, allowing us to probe an ample energy range for energy-dependent hot carrier generation and injection. We used five different light emitting diodes (LEDs) and two lasers as light sources with energies ($\hbar\omega$) ranging from 1.6 to 2.4 eV. The angle-dispersive response for a Ag/TiO_2 heterostructure showed that a range of SPP resonances can be reached by simply altering the incident excitation angle and the photon energy (Figure 1b), without changing the geometry of the plasmonic structure. The normalized LED light spectra (left) and their corresponding angle-dependent reflectivity spectra (bottom) are also shown in Figure 1b. To evaluate a bare metal plasmonic system, the TiO_2 film deposition was omitted and Au was used in place of Ag. Au was used in this case since it is more resistant against oxidation than Ag, and therefore acts as a more stable working electrode for electrochemical evaluation in direct contact with the solution. An angle-dependent dispersion curve for the bare Au film (40 nm thickness) is shown in Electronic Supplementary Information (ESI, Figure S1).

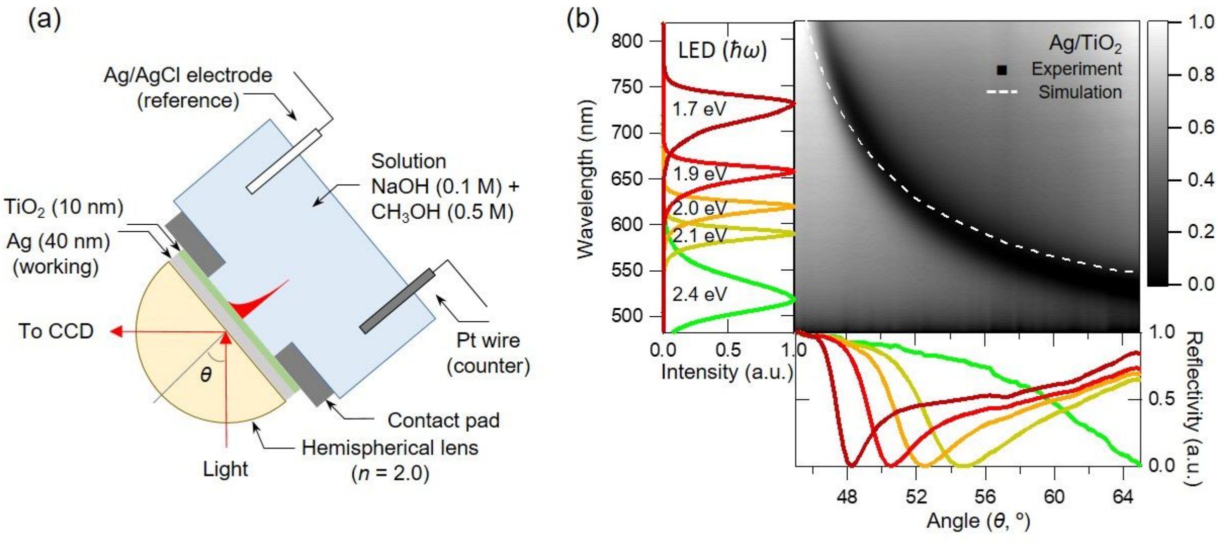

Figure 1. Surface plasmon polariton (SPP)-induced hot carrier generation for photocatalysis. (a) A schematic diagram of the SPP-supporting electrochemical cell that

allows for the SPP-induced energy-tunable hot carrier generation and its direct use for solution chemistry. SPP resonance can be tuned by changing incident angle (θ) of incoming light, while electrochemical responses at the metal – semiconductor or bare metal surface are monitored. (b) SPP dispersion curve for a Ag/TiO_2 heterofilm: Measurement shown in a black and white contour plot (Ag/TiO_2 = 40/10±3 nm in thickness) and simulation in a white dashed line (40/14 nm). Normalized LED light spectra with excitation energies ($\hbar\omega$) from 1.7 to 2.4 eV (left) and corresponding angle-dependent reflectivity spectra (bottom panel) are also shown as a function of θ. A dispersion curve for a Au film (40 nm thickness) is shown in Supporting Information (Figure S1).

Either the metal – semiconductor heterofilm or bare metal film served as a working electrode in a three electrode electrochemical cell consisting of a Pt wire (counter) and Ag/AgCl electrode (reference). The electrochemical response at the working electrode was then recorded in a mixed solution of sodium hydroxide (NaOH;

0.1 M) and methanol (CH_3OH; 0.5 M), or in a NaOH solution (0.1 M) where pH was varied by altering NaOH concentration while maintaining a fixed ionic content with sodium perchlorate ($NaClO_4$). Detailed descriptions about the preparation of the SPP-supporting electrochemical cell and electrochemical measurements can be found in Experimental section.

Tuning of Excitation Angle and Photon Energy in Ag/TiO_2 Heterofilm. First, we verified the incident angle- and energy-dependent photocurrent response of an Ag/TiO_2 heterofilm interfaced with a solution of NaOH and CH_3OH in Figure 2a (see Figure S2 for full angle-dependent chronoamperometry profiles). Five different LEDs with $\hbar\omega$ spanning from 2.4 to 1.7 eV were used to launch SPPs and, subsequently, generate hot carriers. In all cases, positive photocurrents occurred, indicating an oxidation reaction at the working electrode (*i.e.*, holes traveling from the working electrode into solution) and a reduction reaction at the Pt counter electrode (*i.e.*, electron-driven). This is consistent with our earlier study[41] that monitored a hot hole-driven OH^- oxidation. Although Au/TiO_2 heterostructures are often used to selectively collect excited *electrons*, extending their lifetime by keeping them separated from holes,[43,44] the thin TiO_2 layer in our system is expected to be fully depleted of carriers. As such, it will exhibit no band bending or ability to keep carriers separated. Instead, both electrons and holes may be conveyed into the TiO_2. In fact, the exclusive observation of oxidative currents for this metal – semiconductor heterostructure is not surprising since TiO_2 is a well-known catalyst for oxidative chemistries.[3] Therefore, even if both carrier types are present, oxidative processes would be expected to dominate the TiO_2 surface-mediated reactions. Hot hole-driven photoelectrochemical reactions have been also shown in LSP-supporting metal nanoparticles deposited on indium tin oxide, fluorine tin oxide, TiO_2,[45] or gallium nitride,[46] and Au/SiO_2/Au core/shell nanoparticles.[47] However, we note that the TiO_2 layer with no metal film showed no photo-induced electrochemical response,[41] demonstrating the clear role of metal films in creating hot carriers.

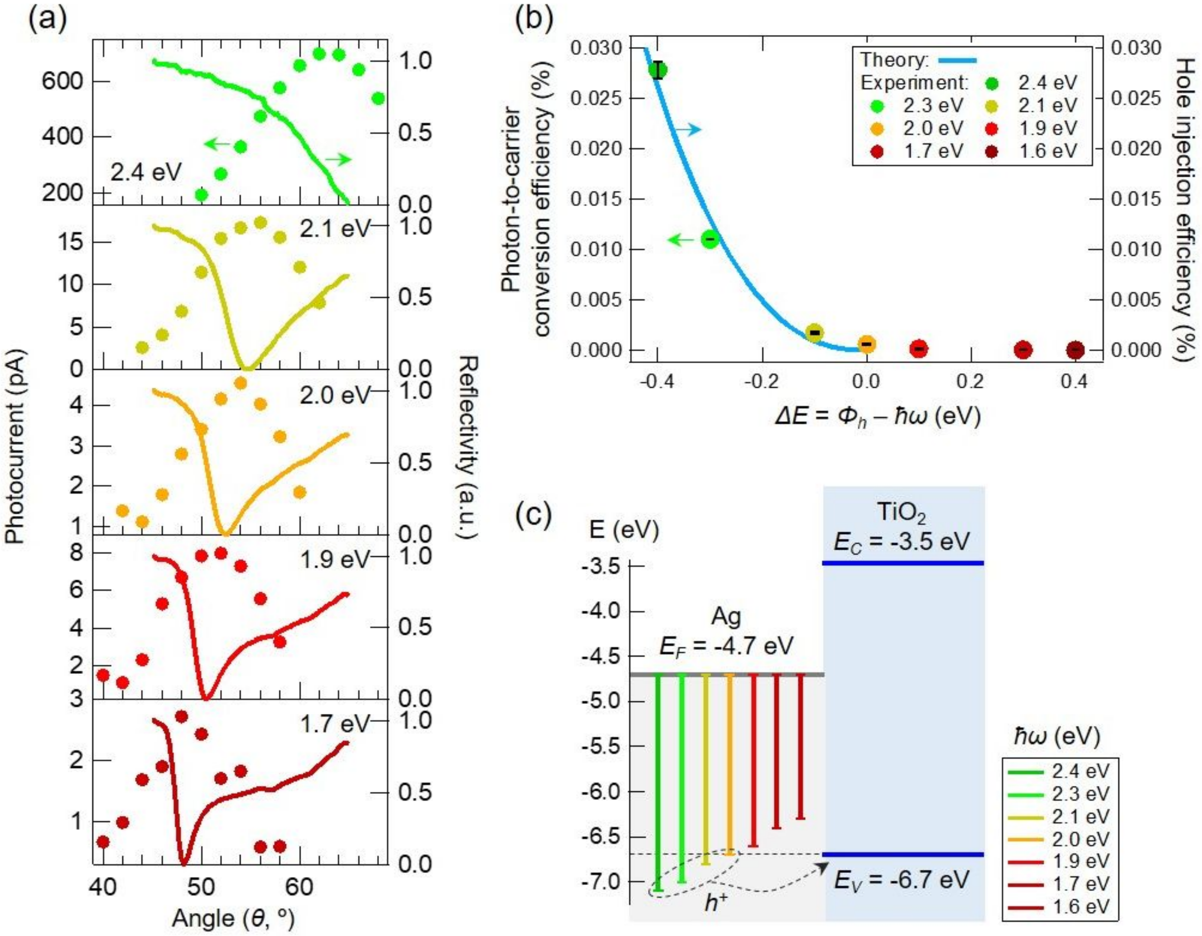

Figure 2. Angle- and energy-dependent photocurrent in a Ag/TiO$_2$ heterofilm. (a) Photocurrents measured in a Ag/TiO$_2$ heterofilm while an illumination angle of the beam was tuned from 40 to 68º (solid circles) were plotted along with angle-dependent reflectivity spectra of five different LED sources having energies from 2.4 to 1.7 eV (solid lines). (b) Experimentally-obtained photon-to-carrier conversion efficiencies obtained with varied excitation energies (solid circles) were plotted with the calculated hole injection efficiency (blue line). Details of the calculation of experimental photon-to-

carrier conversion efficiency and theoretical Schottky transport model can be found in ESI. (c) An energy diagram of the Ag/TiO_2 heterofilm. E_F: Fermi level of Ag, E_C: conduction band, and E_V: valence band of TiO_2. Hot holes created with sufficient photon energy (>2.0 eV) can be transported to the TiO_2 layer, resulting in a chemical reaction. Note that the TiO_2 bands are shifted to give an electron barrier height of 1.2 eV. This barrier height differs from that expected based purely on the work function and electron affinity of the participating materials due to defect-related charges and dipoles generated at the metal semiconductor interface, and is in reasonable agreement with values from the literature.[48,49]

Figure 2a shows a strong dependence of the photocurrent on the incident angle of incoming light. This correlation is verified by the coincidence between the maximum photocurrent (solid circles) and minimum reflection (solid lines) for each light source, both obtained at the SPP resonant angle (θ_{SPP}). Since light is coupled into SPP excitations most efficiently at θ_{SPP}, their decay into hot carriers and the resulting electrochemical currents are also maximized at this optimum angle. We emphasize that the angle dependence in photocurrent was not limited to a single excitation energy, but instead, was observed universally, regardless of excitation energy varying from 2.4 to 1.7 eV. Such an angle dependence confirms that the electrochemical reaction is an SPP-mediated process, and is a clear demonstration that a single SPP-supporting metal – semiconductor heterofilm is capable of generating hot carriers across a wide range of resonance energies simply by changing the incident illumination angle.

Second, we observed that the excitation energy used to create hot carriers on the Ag/TiO_2 heterofilm had a strong influence on the incident-photon to collected-carrier conversion efficiency (Figure 2b). This energy dependence also allowed us to complete the hot carrier transport model developed earlier for the Ag/TiO_2 heterofilm,[41] as we used not just two but multiple light sources in this work (Figure 2c). All light sources used (including two additional lasers with $\hbar\omega$ = 2.3 and 1.6 eV) had energies lower than the interband threshold of Ag (~3.6 eV)[23] and the band gap of TiO_2 (3.2 eV).[3] Therefore, we neglected the effect of interband transitions of charge carriers on photocatalysis. Again, the sign of photocurrents identifies hot hole-driven oxidation in Figures 2a and

S2. Since the highest energy that hot holes may attain is $E_{max} = E_F - \hbar\omega$, where E_F is the Fermi level of the metal, SPP decay can generate energetic holes at energies from -6.3 to -7.1 eV relative to vacuum (color bars in Figure 2c). We expect significant transport of holes over the barrier (and eventually into solution for a reaction) only when the maximum hot-hole energy exceeds the barrier height (*i.e.*, $\hbar\omega > \Phi_h$). This is qualitatively seen when plotting the experimental conversion efficiency (*i.e.*, the measured photocurrents / illumination intensities of light; see ESI for details) as a function of the difference between the estimated Schottky barrier for hole injection (Φ_h = 2.0 eV) and $\hbar\omega$. Generally, the conversion efficiency increased monotonically when the maximum carrier energy exceeds the barrier height and spanned five orders of magnitude from 7.0×10^{-7} % to 0.028 % for $1.6 \leq \hbar\omega \leq 2.4$ eV (solid circles in Figure 2b and details in ESI). Although the focus of our work is not on enhancing or optimizing the photocatalytic efficiency but rather on utilizing the resonance tunability for chemistry, the SPP-supporting system reaches the efficiency of some nanoparticle-based LSPR systems under high energy excitation.[44,50] Nevertheless, the possibility of enhancing photon-to-carrier conversion efficiency in the SPP-supporting system seems plausible based on theoretical and experimental works where the density of surface plasmon modes is increased by periodic texturing of the metal surfaces,[51] the propagation length and light confinement are both enhanced by designing metal-insulator-metal structures,[52] and the electromagnetic field intensity is enhanced by coupling LSP-supporting metal nanoparticles to SPP-supporting metal films.[53]

The measured conversion efficiency *vs*. photon energy compares well with a Schottky transport model, which integrates the product of the distribution function for hot-hole generation, the transport efficiency, and the transmission probability at the Ag/TiO_2 interface, assuming momentum conservation parallel to the interface (blue line in Figure 2b and details in ESI). The results are consistent with SPP decay into hot electrons and holes and, while both carrier types may be present and migrate, the hole transport over the Ag/TiO_2 Schottky barrier drives oxidation reactions, which dominate the electrochemical response. Figure 2b also demonstrates the power of the SPP platform for examining mechanisms of plasmonically-driven chemistry, in that a single material system was used to measure the reaction efficiency for plasmons with resonant energies spanning 0.8 eV, and allowed comparison to a mechanistic model. Lastly, although we chose to illuminate with multiple relatively narrow-band sources, for chemical systems with more efficient response, a single white light source could be used with the SPP resonance, and therefore carrier energy, tuned strictly by incident angle.

We also note that low-intensity illumination was used in this work for the generation of hot carriers. Illumination powers at the sample were ~10 μW (the full range of values is listed in ESI) and the maximum LED power used per area of the working electrode (3.9 W/m^2) was less than 1% of solar intensity (1000 W/m^2). This rules out pronounced plasmonic heating, which generally requires an illumination intensity ~10^7 W/m^2 (~10^4 times solar intensity).[54] The linear dependence of photocurrent on illumination power and the estimated temperature increase of <1 °C in our experimental conditions[41] also support that the observed electrochemical reaction follows a photogenerated carrier mechanism rather than plasmon-induced heating. The low-intensity visible-light illumination makes SPP-driven photocatalysis economically accessible and, more importantly, extends its capacity for driving energy-tunable, non-thermal photocatalytic reactions.

Tuning of Solution pH and Electrode Potential in Oxide-Free Au Film. Next, we investigated SPP-induced hot carrier generation for selective chemistry using an oxide-free bare plasmonic metal film. Although the bare metal structure is simpler to fabricate (no ALD of a semiconductor layer is required) and it can reveal the energetic charge transfer at the metal – molecule interface, this system exhibits reduced electrochemical efficiency due to the absence of the oxide film. The oxide coating in the metal – semiconductor heterofilm served primarily as a reservoir for carrier injection and can also help catalyze photoelectrochemical reactions.[3] Therefore, for the oxide-free all-metal structure studied here, we used a 785 nm laser ($\hbar\omega$ = 1.6 eV) as an illumination source and increased our illumination aperture size, yielding an intensity at the sample ~5.0×10^3 W/m^2. This illumination intensity is still 3-4 orders of magnitude less than that required for plasmonic heating.

We characterized both the photovoltage and photocurrent responses of the SPP-supporting Au working electrode interfaced with NaOH solutions of varied pH values and under a range of applied biases. Changing solution pH and electrode potential allows one to tune the relative energies of the chemical redox potential and the metal Fermi level, which selects the chemistry driven by SPP-induced hot-carrier generation. Figure 3a shows photovoltages (*i.e.*, changes in the open-circuit potential upon illumination) of the bare Au film illuminated by the 785 nm laser (gray shades) while the incident angle was tuned from 40 to 56° in solutions with pHs varied from 9 to 13 (from top to bottom). The photovoltage exhibits a noticeable angle dependence, although the increased angular breadth of the incident laser makes this dependence less distinct when compared to that observed for the Ag/TiO_2 films (Figure S3 vs. Figure 2a). More intriguing, however, is the photovoltage sign change when the pH was varied. At pH 9 and 11, negative photovoltages of a few hundred microvolts were observed, which indicates that negative charges were accumulated on the Au working electrode and positive charges were lost to the solution through hot hole-driven oxidation. On the other hand, a clear reversal of the photovoltage sign occurred at solution pH 13, where a hot electron-driven reduction was observed.[55] At pH 13, the form of the current–time trace also substantially changes—at pH 9 and 11, a steady-state potential value is quickly reached, whereas at pH 13, steady-state is still not achieved after 20 seconds. The changes at pH 13 suggest not only a switch to a cathodic charging process, but a change of electrochemical reaction dominating the charging of the electrode.

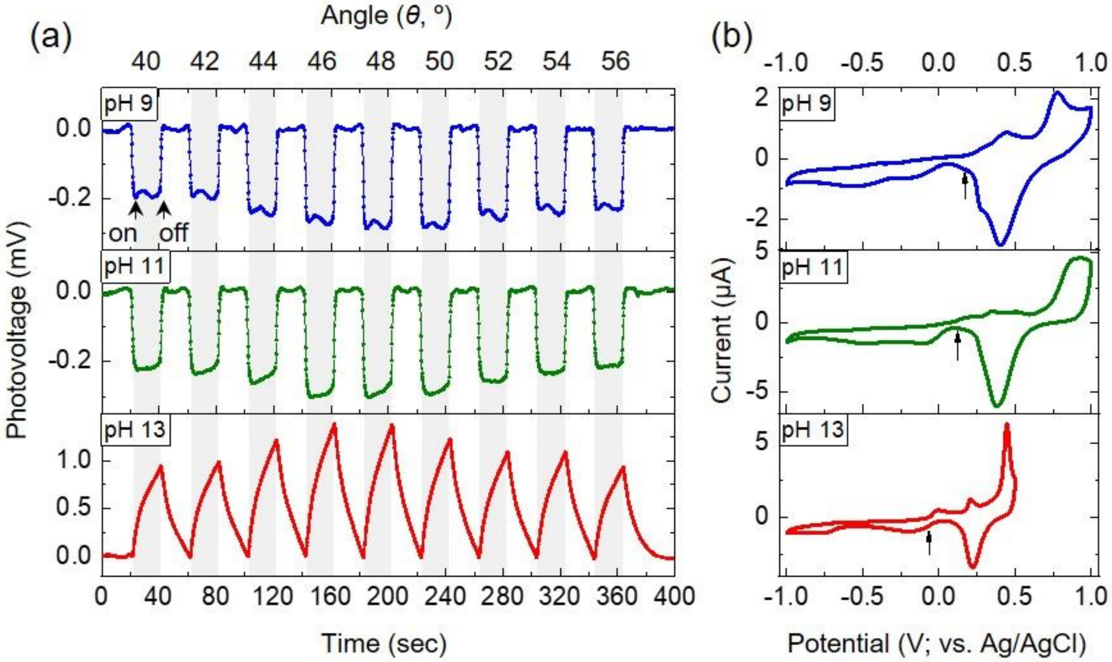

Figure 3. Solution pH-dependent photovoltage in a bare Au film. (a) Photovoltage and (b) cyclic voltammetry (CV) responses of a bare Au film at a varied solution pH from 9 to 13. Photovoltages were measured while the incident angle of the 785 nm laser was tuned from 40 to 56°. Gray shaded areas indicate light illumination and white background areas dark conditions (light turned off). CV curves were obtained in the dark

at a scan speed of 50 mV/sec. Black arrows indicate open circuit potential measured at each pH.

In order to identify the redox chemistry associated with the observed photovoltages, we compared these results to cyclic voltammetry (CV) responses of a bare Au film that was prepared separately on a cover glass under the same metal evaporation condition and exposed to de-aerated NaOH solutions of varying pH (Figure 3b). Rather than mass spectrometry or optical techniques such as Raman spectroscopy, CV was used to analyze possible chemical reactions and reaction products. This is because there are several electrochemical reactions that can occur at Au under the experimental conditions applied. Various forms of Au oxides can form in NaOH solution, which are difficult to distinguish with spectral information given by mass spectrometry or Raman spectroscopy, but can be identified with reduction potentials databased for specific reactions in solution. Additionally, oxidation of solution OH^- species is readily accessible under basic conditions (Equation 1):

$$4\ OH^{-} \rightarrow O_2 + 2\ H_2O + 4\ e^{-} \qquad [1]$$

The main features in the CV curves are dominated by surface electrochemical processes. The broad pre-oxidation region associated with adsorption/desorption of OH^{-} ions, and the pronounced anodic and cathodic peaks, are attributed to oxide layer formation and reduction, respectively.[56,57] The complex current – voltage *(I – V)* behavior of the Au films in dark and illuminated conditions can be partially explained by Equations 2–4. The first anodic wave (at potential > ~0.25 V) at all three pH values is due to the formation of surface hydroxides and oxides of various stoichiometry [Eqns. 2–4]; the second anodic wave derives from formation of hydrous oxides with the concomitant production of oxygen [Eqn. 4].[56,57] These oxidation reactions are nearly all accompanied by release of protons, and thus shift to more negative potentials as pH increases.

$$2\ Au + 3\ H_2O \rightarrow Au_2O_3 + 6\ H^{+} + 6\ e^{-} \qquad [2]$$

$$Au + H_2O \rightarrow Au^{\delta+}OH^{\delta-} + H^{+} + e^{-} \rightarrow \cdots \rightarrow Au(OH)_3 + x\ H^{+} + x\ e^{-} + x\ H_2O \qquad [3]$$

$$Au_2O_3 + H_2O \rightarrow Au_2O_3{\cdot}H_2O \rightarrow 2\ AuO_2 + 2\ H^{+} + 2\ e^{-} + O_2$$

[4]

We posit that all reaction pathways are accessible at pH 9, 11, and 13. The steady-state form of the current–time traces at pH 9 and 11 suggests that the dominating anodic reaction is oxidation of solution-phase $OH^–$ [Eqn. 1], as the solution-phase reaction does not involve kinetically slow formation or dissolution of surface oxides. The electrochemical oxidation of $OH^–$ is readily accessible at modest potentials. The standard potential (E^0) for this reaction is 0.401 V (vs. SHE) at pH 0,[58] which shifts to -0.130 V, -0.248 V, and -0.366 V at pH 9, 11, and 13, respectively. At pH 13, the kinetically slow, positive-going potential change implies switching to domination by a slower cathodic process at the Au surface. It should also be noted that the open-circuit potential of the illuminated electrode changes by ~-0.2 mV at pH 9 and 11, while that at pH 13, the potential shift is ~+1.0 mV, again implying a different electrochemical process predominates at pH 13.

The broad cathodic waves at potentials negative of 0 V in the CV obtained at the Au electrodes (Figure 3b) correspond to the reduction of hydrous gold oxides (reverse of the reaction sequence in Eqn. 4). These features remained after the Au electrode was stabilized over multiple CV cycles in a de-aerated NaOH solution (Figure S4). As pH was adjusted from 9, 11, to 13, open-circuit potential values shifted from +0.17, +0.12, to -0.06 V (indicated as black arrows), approaching the redox feature associated with the reduction of hydrous gold oxides, thus resulting in a photovoltage sign change at pH 13 relative to those obtained at pH 9 and 11. As pH increases, the redox potentials on the Au surface shift negatively, and at pH 13, the cathodic wave derived from reduction of hydrous metal oxides overlaps with the metal Fermi level under illumination, causing the onset of a cathodic photocurrent (Figure 3b). This coincidence of Fermi level and cathodic CVs features further supports the switch to domination by cathodic electrochemistry at pH 13 as well as onset of dominance of the charging process by kinetically slow reduction of surface oxides, as implied by the change of form in the current–time traces in Figure 3a. By tuning the redox potential of the molecular system *via* pH, both hot hole- and hot electron-driven processes could be selected in the bare metal film. Although we do not show pH-dependent results for the metal – semiconductor heterofilm system, we suspect it would strongly favor oxidative reactions originating with TiO_2 surface-mediated oxidation catalysis.[3]

We pursued additional control of the resulting chemical reactions by tuning both the Fermi level of the metal (*via* electrode potential variation) and the redox potential of the molecules (*via* solution pH variation) while electrochemical photocurrents were measured (Figure 4; see Figure S5 for the full angle-tuned photocurrent profiles of the bare Au film). First, the Fermi level of the Au film (located -5.1 eV relative to the vacuum) was tuned by applying a bias to the working electrode (indicated as color bars relative to the Ag/AgCl reference) at a pH of (a) 9, (b) 11, and (c) 13. Taking pH 13 as an example (Figure 4c), an increased electron energy at a negative potential of -0.25 V relative to Ag/AgCl (blue) caused the electron transfer from the Au electrode to the solution resulting in a cathodic photocurrent (reduction), while applying a positive potential of +0.34 V (red) caused electrons in the solution to transfer to the Au electrode, resulting in an anodic photocurrent (oxidation). Similar photocurrent responses were shown at pH 9 and 11, with electrode potentials tuned relative to the redox potential of the molecule. Sharp anodic or cathodic spikes appeared upon light on/off are attributed to surface charging – discharging effects.[59] The photocurrent response also showed a strong pH-dependence; under comparable biases applied to the Au electrode (red), positive photocurrents increased ~2 orders of magnitudes at pH 13 compared with pH 9, a direct consequence of shifting redox energies relative to the electrode's Fermi level. In general, the photocurrent results (Figure 4a-c) correlate well with the photovoltage results (Figure 3a) at the different pH values, wherein the photocurrents observed at pH 13 are both larger than those obtained at pH 9 and 11, and fail to reach steady state. The photocurrent results further support the assertion that the surface-oxide reduction processes dominate the photoelectrochemical response at pH 13.

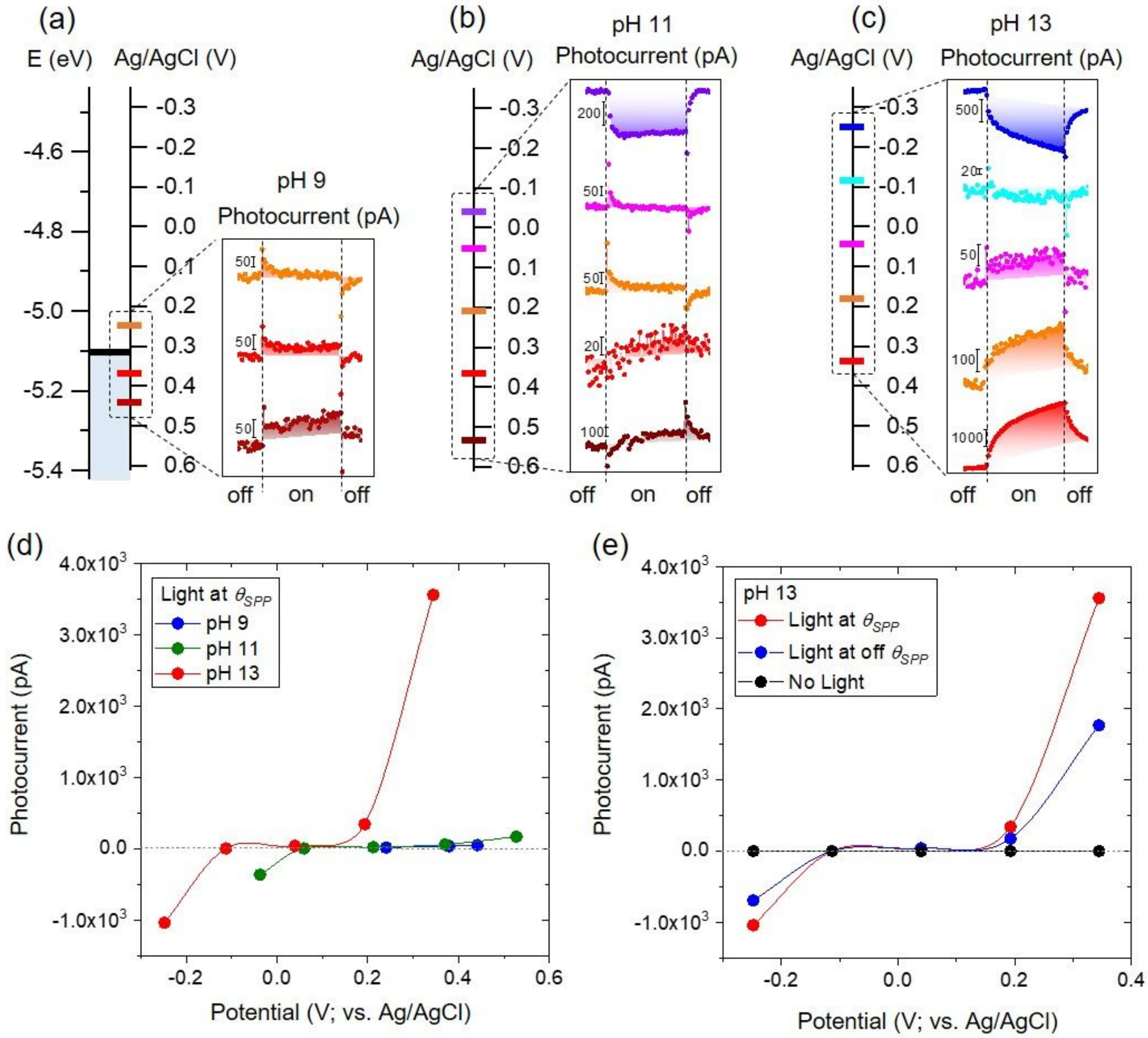

Figure 4. Solution pH- and electrode potential-dependent photocurrent in a bare Au film. Dependence of photocurrents on the varied solution pHs from (a) 9, (b) 11, to (c) 13, and electrode potential (color bars) in a bare Au film upon a 785 nm laser irradiation at θ_{SPP}. $I - E$ curves for the bare Au film (d) at a fixed angle (θ_{SPP}) and varied solution pHs from 9 to 13, and (e) at a fixed pH 13 with the incident light at θ_{SPP} (46º; red), off θ_{SPP} (40º; blue), and no light irradiation (black).

Finally, bias- and pH-dependent photocurrents yielded the photocurrent – potential (I – E) curve in Figure 4d. The I – E curve revealed that at pH 13, the onset potential for oxidation is ~0.136 V. This onset potential shifts positively for decreasing pH values, consistent with the enhanced oxidative currents at a given bias as pH increases (Figure 4a-c). We further confirmed that both reduction and oxidation photocurrents are due to hot carriers generated by SPP decay by plotting the I – E curves of the bare Au film electrode with light irradiation at the SPP resonant angle (θ_{SPP} = 46°; red), off-resonant angle (40°; blue), and with no illumination (black) in Figure 4e. The highest photocurrents were obtained at θ_{SPP} and no photocurrents were obtained in the dark condition, demonstrating that the photocurrents are due to the hot carriers generated by SPP decay. The reduced but measurable photocurrents at the off-resonant angle were attributed to angularly broadened illumination associated with the increased aperture size, which dampens the angular dependence of photocurrents (see also Figure 3a).

The inversion of the photocurrent direction upon the variation of the applied bias and solution pH is a direct indication that by tuning the relative energies of the electrode and reaction potential we can control the transport of the SPP-generated hot carriers within the working electrode. While this is similar to conventional CV, we are exclusively probing carriers generated *via* plasmon decay in order to selectively drive either cathodic (reduction) or anodic (oxidation) photocurrents. This ambipolar response is a consequence of using a homostructure. The potential energy barriers in some heterostructure systems, assuming a semiconductor that is not fully depleted, provide a means for immediate charge separation, extending hot-carrier lifetime and enabling their collection as electrochemical current.[21] The all-metal homostructure has no such internal potential barriers, so the initially excited carriers are not separated. Instead, they rapidly thermalize near the Fermi level,[60] where they can be motivated to participate in redox chemistry *via* applied potential. These system considerations are consistent with our results. The reactions observed for the all-metal system (Figures 3 and 4) occur near the potentials expected for conventional electrochemistry, which suggests that the carriers responsible for the electrochemical currents are energetically positioned near the Fermi level. On the other hand, the data associated with the metal – semiconductor heterostructure (Figure 2 and results in Ref. 41) are consistent with collection of hot carriers located as far as $\hbar\omega$ below the Fermi level. We believe this distinction is a direct result of the hetero- versus homostructure nature of the systems.

Conclusions

The ability to generate hot carriers with energy tunability provides an exciting opportunity for creating photocatalysis designs for selected chemical reactions. It was demonstrated that the generation and injection of hot carriers can be tuned in a SPP-supporting metal – semiconductor heterofilm or all-metal film through the systematical tuning of the excitation energy, solution pH, and electrode potential. With the continuous spectral tunability of the SPP system, hot carriers were generated over a wide range of visible wavelengths without changing geometry, materials, or the environment of the system, all of which would likely alter the chemical processes under examination. This work and future studies on the SPP-generated carrier transport are expected to greatly increase our understanding of the plasmon-induced photocatalysis and guide design for selective photocatalysis.

Experimental section

Fabrication of Surface Plasmon Polariton (SPP)-Supporting Electrochemical Cell. The Kretschmann geometry was used to launch SPPs at the plasmonic metal film – dielectric interface using a high-index hemispherical lens (n = 2.0, diameter = 10.0 mm; Edmund Optics). A flat side of the hemispherical lens was deposited with Cr (adhesion layer) / Au (or Ag) films (thickness = 2 / 40 nm) *via* electron beam evaporation (Model FC-2000, Temescal Systems). In order to create metal – semiconductor heterofilms, a TiO_2 film (10±3 nm thickness, anatase crystalline structure confirmed by Raman measurements[41]) was deposited on top of a Ag film *via* atomic layer deposition (TDMAT / O_2 precursors with N_2 purge at 300ºC; ALD System, Oxford Instruments). For the all-metal plasmonic system, TiO_2 film deposition was omitted and Au was used in place of Ag. An incident angle of incoming light to the hemispherical lens was tuned using a custom-built sample rotator (BGM80, Newport) from 40 to 68°.

Electrochemical Measurements. The prepared Ag/TiO_2 heterofilm or bare Au film served as a working electrode in a three-electrode electrochemical cell consisting of a Pt wire (counter) and Ag/AgCl electrode (reference). The electrochemical response at the working electrode was recorded using a potentiostat (Gamry Instruments) in a mixed solution of sodium hydroxide (NaOH, Sigma-Aldrich; 0.1 M) and methanol (CH_3OH, Fisher Chemical; 0.5 M), or in a NaOH solution where pH was varied by altering NaOH concentration while maintaining a fixed ionic content with sodium perchlorate ($NaClO_4$, Alfa Aesar). For example, we prepared solutions of 1.0×10^{-3} M NaOH + 9.9×10^{-2} M $NaClO_4$, and 1.0×10^{-5} M NaOH + 1.0×10^{-1} M $NaClO_4$, for pH 11 and 9, respectively. Solutions of 0.1 M NaOH were prepared for pH 13. During the initial calibration, the prepared solution was bubbled with N_2 for ~1 hour to remove

O_2 dissolved in the solution, and electrochemical measurements were performed under a blanket of N_2.

Light Sources. Several light emitting diodes (LEDs; Thorlabs) with energies varying from 1.7 to 2.4 eV, as well as two lasers with energies of 1.6 eV (OEM Laser Systems) and 2.3 eV (Blue Sky Research FiberTec) were used as light sources in our experiments. The wavelengths and linewidths of each LED are 519.2±39.5, 590.0±13.6, 619.7±14.4, 658.1±18.0, and 732.2±29.4 nm (normalized LED light spectra are shown in the left panel of Figure 1b). A plano-convex lens, collimation lens, and level-actuated iris (all from Thorlabs) were used to collimate the beam to the hemispherical lens. The illumination power of the LED or laser was measured using an optical power meter (842-PE, Newport).

SPP Dispersion Curve: Experiment. Light reflectivity from the hemispherical lens deposited with a metal – semiconductor heterofilm or a bare metal film was recorded using an imaging spectrometer (Andor Shamrock) and a high-resolution imaging CCD (iXon^{EM} Andor Technology), while incident angle of white light (Halogen HL-2000-FHSA, Ocean Optics) was continuously tuned. The reflectivity spectra were compiled using custom-written Igor scripts (Igor Pro. v6.3.7.2.) to plot SPP dispersion curves as a function of incident angle of light versus wavelength. For normalization, the white light spectrum was taken from the white light reflected by a silver mirror under the same acquisition condition.

SPP Dispersion Curve: Simulation. Reflectivity as a function of incident angle was also obtained using a transfer matrix calculation. Each layer of the multilayer (glass, Cr, Au or Ag, TiO_2, water) was defined by its thickness and dielectric function. The dielectric function of the hemispherical lens was taken as lossless, with a spectrally-independent refractive index of 2. The spectrally-dependent dielectric function of Cr and TiO_2 were taken from the WVASE software package.[61] The optical constants for Au and Ag were gratefully taken from ab initio calculations.[62]

Conflicts of interest

There are no conflicts to declare.

Acknowledgements

This research was performed while the author, Wonmi Ahn, held a National Research Council (NRC) Research Associateship award at the U.S. Naval Research Laboratory. The work was supported by the Office of Naval Research and the U.S. Naval Research Laboratory.

Electronic Supplementary Information (ESI) available. Experimental photon-to-carrier conversion efficiency in a Ag/TiO_2 heterofilm, calculation of hole conversion efficiency using a Schottky transport model, SPP dispersion curve of a bare Au film, angle-dependent photocurrents measured in a Ag/TiO_2 heterofilm with varied excitation energies, solution pH-dependent photovoltage in a bare Au film, cyclic voltammetry curves of a bare Au film, dependence of photocurrents on solution pH and electrode potential in a bare Au film.

Corresponding Author

*E-mail: *blake.simpkins@nrl.navy.mil*

Notes and references

(1) J. Kou, C. Lu, J. Wang, Y. Chen, Z. Xu and R. S. Varma, *Chem. Rev.* 2017, **117**, 1445 – 1514.

(2) A. Testino, I. R. Bellobono, V. Buscaglia, C. Canevali, M. D'Arienzo, S. Polizzi, R. Scotti and F. Morazzoni, *J. Am. Chem. Soc.* 2007, **129**, 3564 – 3575.

(3) A. L. Linsebigler, G. Lu and J. T. Yates, Jr., *Chem. Rev.* 1995, **95**, 735 – 758.

(4) B. Kraeutler, C. D. Jaeger, and A. J. Bard, *J. Am. Chem. Soc.* 1978, **100**, 4903 – 4905.

(5) A. L. Attwood, J. L. Edwards, C. C. Rowlands and D. M. Murphy, *J. Phys. Chem. A.* 2003, **107**, 1779 – 1782.

(6) R. Asahi, T. Morikawa, T. Ohwaki, K. Aoki and Y. Taga, *Science* 2001, **293**, 269 – 271.

(7) T. Hirakawa and Y. Nosaka, *J. Phys. Chem. C.* 2008, **112**, 15818 – 15823.

(8) L. Ren, M.-M. Yang, C.-H. Tung, L.-Z. Wu and H. Cong, *ACS Catal.* 2017, **7**, 8134 – 8138.

(9) J. Li, J. P. McClure, R. Fu, R. Jiang and D. Chu, *Appl. Surf. Sci.* 2018, **429**, 48 – 54.

(10) X. Zhang, X. Li, D. Zhang, N. Q. Su, W. Yang, H. O. Everitt and J. Liu, *Nat. Commun.,* 2017, **8**, 14542.

(11) Q. Xiao, S. Sarina, E. R. Waclawik, J. Jia, J. Chang, J. D. Riches, H. Wu, Z. Zheng and H. Zhu, *ACS Catal.* 2016, **6**, 1744 – 1753.

(12) X. Ke, S. Sarina, J. Zhao, X. Zhang, J. Chang and H. Zhu, *Chem. Commun.* 2012, **48**, 3509 – 3511.

(13) H. Zhu, X. Ke, X. Yang, X. Sarina and H. Liu, *Angew. Chem. Int. Ed.* 2010, **49**, 9657 – 9661.

(14) C.-H. Hao, X.-N. Guo, Y.-T. Pan, S. Chen, Z.-F. Jiao, H. Yang and X.-Y. Guo, *J. Am. Chem. Soc.* 2016, **138**, 9361 – 9364.

(15) J. Bi, Z. Zhou, M. Chen, S. Liang, Y. He, Z. Zhang and L. Wu, *Appl. Surf. Sci.* 2015, **349**, 282 – 298.

(16) X. Zhang, X. Ke and J. Yao, *J. Mater. Chem. A.* 2018, **6**, 1941 – 1966.

(17) U. Aslam, S. Chavez and S. Linic, *Nat. Nanotechnol.*, 2017, **12**, 1000 – 1005.

(18) H. Robatjazi, H. Zhao, D. F. Swearer, N. J. Hogan, L. Zhou, A. Alabastri, M. J. McClain, P. Nordlander and N. J. Halas, *Nat. Commun.,* 2017, **8**, 27.

(19) S. Link and M. A. El-Sayed, *J. Phys. Chem. B.* 1999, **103**, 8410 – 8426.

(20) U. Kreibig and M. Vollmer, Optical Properties of Metal Clusters, Springer-Verlag Berlin, Heidelberg, 1995; pp 94 – 95.

(21) K, Marchuk and K. A. Willets, *Chemical Physics* 2014, **445**, 95 – 104.

(22) W. Li and J. G. Valentine, *Nanophotonics*, 2017, **6**, 177 – 191.

(23) R. Sundararaman, P. Narang, S. A. Jermyn, W. A. Goddard III and H. A. Atwater, *Nat. Commun.,* 2014, **5**, 5788.

(24) A. M. Brown, R. Sundararaman, P. Narang, W. A. Goddard III and H. A. Atwater, *ACS Nano* 2016, **10**, 957 – 966.

(25) M. Bernardi, J. Mustafa, J. B. Neaton and S. G. Louie, *Nat. Commun.* 2015, **6**, 7044.

(26) H. Zhang and A. O. Govorov, *J. Phys. Chem. C.* 2014, **118**, 7606 – 7614.

(27) L. V. Besteiro and A. O. Govorov, *J. Phys. Chem. C.* 2016, **120**, 19329 – 19339.

(28) J. J. Mock, M. Barbic, D. R. Smith, D. A. Schultz and S. Schultz, *J. Chem. Phys.* 2002, **116**, 6755 – 6759.

(29) Z. Zheng, B. Huang, X. Qin, X. Zhang, Y. Dai and M.-H. Whangbo, *J. Mater. Chem.* 2011, **21**, 9079 – 9087.

(30) X. Ke, X. Zhang, J. Zhao, S. Sarina, J. Barry and H. Zhu, *Green Chem.* 2013, **15**, 236 – 244.

(31) C. Boeigter, R. Campana, M. Morabito and S. Linic, *Nat. Commun.* 2016, **7**, 10545.

(32) S. Linic, U. Aslam, C. Boerigter and M. Morabito, *Nat. Mater.* 2015, **14**, 567 – 576.

(33) C. G. Silva, R. Juárez, T. Marino, R. Molinari and H. García, *J. Am. Chem. Soc.* 2011, **133**, 595 – 602.

(34) F. Wu, X. Hu, J. Fan, E. Liu, T. Sun, L. Kang, W. Hou, C. Zhu and H. Liu, *Plasmonics* 2013, **8**, 501 – 508.

(35) J.-W. Park and J. S. Shumaker-Parry, *J. Am. Chem. Soc.* 2014, **136**, 1907 – 1921.

(36) J.-W. Park and J. S. Shumaker-Parry, *ACS Nano*, 2015, **9**, 1665 – 1682.

(37) S. E. Skrabalak, L. Au, X. Li and Y. Xia, *Nat. Protoc.,* 2007, **2**, 2182 – 2190.

(38) I. Tokarev, I. Tokareva and S. Minko, *Adv. Mater.* 2008, **20**, 2730 – 2734.

(39) B. M. Crockett, A. W. Jansons, K. M. Koskela, D. W. Johnson and J. E. Hutchison, *ACS Nano*, 2017, **11**, 7719 – 7728.

(40) C. Sönnichsen, B. M. Reinhard, J. Liphardt and A. P. A. Alivisatos, *Nat. Biotechnol.*, 2005, **23**, 741 – 745.

(41) W. Ahn, D. C. Ratchford, P. E. Pehrsson and B. S. Simpkins, *Nanoscale* 2017, **9**, 3010 – 3022.

(42) M. R. Saleem, R. Ali, M. B. Khan, S. Honkanen and J. Turunen, *Frontiers in Materials* 2014, **1**, 1 – 15.

(43) Y. Tian and T. Tatsuma, *J. Am. Chem. Soc.* 2005, **127**, 7632 – 7637.

(44) Z. Bian, T. Tachikawa, P. Zhang, M. Fujitsuka and T. Majima, *J. Am. Chem. Soc.*, 2014, **136**, 458 – 465.

(45) E. S. Thrall, A. P. Steinberg, X. Wu and L. E. Brus, *J. Phys. Chem. C.* 2013, **117**, 26238 – 26247.

(46) J. S. DuChene, G. Tagliabue, A. J. Welch, W.-H. Cheng and H. A. Atwater, *Nano Lett.* 2018, **18**, 2545 – 2550.

(47) A. E. Schlather, A. Manjavacas, A. Lauchner, V. S. Marangoni, C. J. DeSantis, P. Nordlander and N. J. Halas, *J. Phys. Chem. Lett.* 2017, **8**, 2060 – 2067.

(48) F. Hossein-Babaei, M. M. Lajvardi and N. Alaei-Sheini, *Appl. Phys. Lett.* 2015, **106**, 083503.

(49) H. Lee, Y. K. Lee, E. Hwang and J. Y. Park, *J. Phys. Chem. C.* 2014, **118**, 5650 – 5656.

(50) C. Ng, J. J. Cadusch, S. Dligatch, A. Roberts, T. J. Davis, P. Mulvaney and D. E. Gómez, *ACS Nano* 2016, **10**, 4704 – 4711.

(51) S. C. Kitson, W. L. Barnes and J. R. Sambles, *Phys. Rev. Lett.* 1996, **77**, 2670 – 2673.

(52) J. A. Dionne, L. A. Sweatlock, H. A. Atwater and A. Polman, *Phys. Rev. B* 2006, **73**, 035407.

(53) J. J. Mock, R. T. Hill, Y.-J. Tsai, A. Chilkoti and D. R. Smith, *Nano Lett.* 2012, **12**, 1757 – 1764.

(54) M. J. Kale, T. Avanesian and P. Christopher, *ACS Catal.*, 2014, **4**, 116 – 128.

(55) Note that these fundamental processes (electron or hole accumulation on the electrode side of the electrode/electrolyte interface) lead to a counter-intuitive sign difference between open circuit photovoltages and closed-circuit photocurrents under illumination. *I.e.,* oxidizing solution species under open circuit conditions—which initially requires positive electrode potential relative to the solution—causes electron accumulation and concomitantly increasingly negative potential on the electrode side until the electrode voltage reaches a quasi-equilibrium (a photo-stationary state) with

the solution potential. The opposite happens when photoreduction of solution species occurs—holes accumulate at the electrode surface and the open circuit potential becomes more positive.

(56) L. D. Burke and P. F. Nugent, *Gold Bulletin*, 1997, **30**, 43 – 53.

(57) L. D. Burke and L. M. Hurley, *J. Solid State Electrochem.* 2002, **6**, 101 – 110.

(58) D. R. Lide, Handbook of Chemistry and Physics, 76th Ed., CRC Press, New York, 1995 – 1996; pp. 8 – 24.

(59) P. Salvador and C. Gutiérrez, *J. Electroanal. Chem.* 1984, **160**, 117 – 130.

(60) C. Frischkorn and M. Wolf, *Chem. Rev.* 2006, **106**, 4207 – 4233.

(61) WVASE Software Package, J.A. Woollam Co., Inc.

(62) A. M. Brown, R. Sundararaman, P. Narang, W. A. Goddard III and H. A. Atwater, *Phys. Rev. B.* 2016, **94**, 075120.

Table of contents

Hot carrier generation by surface plasmon polariton was demonstrated in a metal/semiconductor heterofilm and a bare metal film for energy-tunable photocatalysis.